Simultaneous Observation of Melt Flow and Motion of Equiaxed Crystals During Solidification Using a Dual Phase Particle Image Velocimetry Technique. Part II: Relative Velocities

ABDELLAH KHARICHA, MIHAELA STEFAN-KHARICHA, ANDREAS LUDWIG, and MENGHUAI WU

A two-camera Particle Image Velocimetry (PIV) technique is applied to study the flow pattern and the equiaxed crystal motion during an equiaxed/columnar solidification process of Ammonium Chloride in a die cast cell. This technique is able to measure simultaneously the liquid and the equiaxed grain velocity pattern as already shown in Part I of this paper. The interaction between the equiaxed grains and the melt flow was explored by means of relative velocities. In single isolated configurations, the settling velocity of equiaxed crystal was found to be 41 times smaller than spheres of equivalent size. The coupling between the fluid flow and the equiaxed crystals was found to be important in areas of high crystal density. Chaotic and turbulent behaviors are found to be damped in regions of high equiaxed crystal density.

DOI: 10.1007/s11661-012-1415-y

I. INTRODUCTION

SOLIDIFICATION is a multidisciplinary field involving thermodynamics, fluid dynamics and solid mechanics, heat and mass transfer, and other disciplines.[1–3] One of the most challenging problems in solidification modeling is the complex interactions between physical phenomena occurring at different length scales ranging from atomic rearrangement over single crystal-melt interactions to heat extraction, momentum and species transport at the system level.

An important phenomenon in solidification is the simultaneous occurrence of melt flow and crystal motion. Solidification takes place either by a growing columnar front and/or by the growth of equiaxed crystals. Columnar growth happens in the form of cells or dendrites from the mold walls into the bulk melt due to heat extraction from outside. In equiaxed solidification, globular or dendritic crystals form by nucleation or fragmentation and subsequent growth into the surrounding melt. When equiaxed solidification is present, the phases (liquid and equiaxed crystal) interact with each other through momentum and energy exchange. The resulting solid–liquid multiphase flow pattern strongly depends on the microstructure of the equiaxed crystals, which in turn is governed by grain nucleation and growth mechanisms. Because the coupled liquid–solid flow causes structural and chemical heterogeneities in the final solidified products, a fundamental understanding of the multiphase transport phenomena coupled with the grain nucleation and growth mechanisms is required. The occurrence of dispersed two-phase flows in nature and industrial applications is abundant. The present topic shows the interaction of solid particles (equiaxed crystals) and the melt flow. However, there is a lack of consistent data to support the numerous theories for flow-particle interaction that have been developed in recent years.[4–9]

Due to its transparency, the H_2O-NH_4Cl solution was used for many experimental studies in the past[1–3,6,10] as the perfect analog for metallic alloys solidification. Beckermann's group used hypereutectic alloys of H_2O-NH_4Cl to study the solidification and the convection phenomena.[11–13] The shadowgraph technique was used in this publication[11] for qualitative comparison between experimental measurements and numerical simulations. On the other hand, a carefully applied analysis of shadowgraph images could as well provide information about the distribution and sizes of grains in the liquid melt at least for small fractions of solid.

A brief introduction to the PIV technique is given elsewhere.[14–17] The current authors described in more detail the principals of the PIV technique in Part I of this paper.

If PIV recordings are evaluated in the conventional way, the resulting velocity value is affected by the signals from the two different phases. The results would probably be a sort of average of the two velocities. Therefore, the signal arising from the individual phases must be separated so that relative velocity can be determined. For the present paper, the relative velocities between melt and crystals have been extracted. Moreover, the influence on the liquid flow of the equiaxed crystals' movement was analyzed.

The technique used here for distinguishing between the two different signals employs fluorescent tracer particles.[18,19] The fluorescent tracers scatter the light at

ABDELLAH KHARICHA, Research Team Leader, MIHAELA STEFAN-KHARICHA, Ph.D. Student, ANDREAS LUDWIG, Professor, MENGHUAI WU, Associate Professor, are with the Department of Metallurgy, University of Leoben, Leoben, Austria. Contact e-mail: abdellah.Kharicha@notes.unileoben.ac.at
Manuscript submitted March 23, 2012.
Article published online September 19, 2012

a wavelength different from that scattered by the equiaxed crystals. The use of two cameras is necessary. The first camera mounted with a green filter (band pass filter of 532 nm) detects only the laser light scattered by the equiaxed crystals. The second camera uses an orange filter (570 nm) through which the light reemitted by the fluorescent dye (Rhodamine B) can be recorded. In the past, this technique was successfully applied to two-phase water-bubble flows with simultaneous separation and measurement of the different phases.

II. EXPERIMENTAL PROCEDURE

For our quantitative study of the interaction between melt flow and solidification, we have chosen the relatively thin rectangular cavity ($10 \times 10 \times 1$ cm^3), which was cooled from three sides with a predefined cooling rate. A hypereutectic H_2O-29.5 wt pct NH_4Cl solution was solidified under controlled conditions. The process was monitored with a two-camera PIV device, whereby a 1-mm-thick cross section in the middle of the test cell was illuminated from the top by Nd-YAG laser pulses.

The cell was made of brass with 1-mm-thick glass plates in the front and at the back. Inside the brass walls, cooling channels which follow a meandering path were designed to achieve a homogeneous temperature. The cooling was controlled by pumping water with a given temperature through the cooling channels.

The H_2O-NH_4Cl solution was prepared by mixing NH_4Cl powder with distillate water and heating to 318.15 K (45 °C) until the powder had completely dissolved. According to the H_2O-NH_4Cl phase diagram, the liquidus temperature of an alloy containing 29.57 wt pct NH_4Cl is 310.15 K (37 °C). Then, fluorescent tracer particles (polyamide particle colored with the Rhodamine B) were added, whereby the solution was intensively stirred. The average diameter of the particles was estimated to be around 10 μm and their material density was around 1.05 g/cm^3. The density of a H_2O-29.5 wt pct NH_4Cl solution at liquidus is about 1.078 g/cm^3 and that of a eutectic H_2O-NH_4Cl solution is 1.076 g/cm^3. Thus, particles and solution have a similar density (difference 2.7 pct for a 29.5 wt pct and 2.5 pct for the eutectic solution), and it is reasonable to assume that the particles follow correctly the flow of the solution. Even if we have a change in temperature during the process, we believe that the change in density is not major.

After having added the particles, the liquid H_2O-NH_4Cl solution is then poured into the preheated die casting cell at 317.15 K (44 °C). This was done slowly in order to prevent capturing air bubbles. Nevertheless, if air bubbles stacked to the cell walls, they were mechanically removed carefully. The filling height was kept at 8 cm. After filling, we waited typically for one hour to equilibrate the temperature field before we started cooling. In this time, the small, but continuous, heat loss through the front and back window resulted in a steady and symmetric thermal buoyancy flow which was used as a reproducible initial stage for the different experimental runs. Then, the brass cell walls were cooled by 1.2 K (1.2 °C)/min. The temperature of the brass walls and at the top middle position in the solution was recorded every 5 seconds with type k thermocouple (accuracy ±0.1 K (±0.1 °C). In order to avoid condensation of humidity on the glass plates, we stopped cooling when 278.15 K (5 °C) was reached. According to the H_2O-NH_4Cl phase diagram, this corresponds to a solid fraction of 30 pct. Thus, the solidification process terminated with a partly solidified cell.

The two-camera PIV system adopted in this study comprised a pulsed laser system for illumination, two CCD cameras for image acquisition, a synchronization unit, and a software packet for image and data processing. The laser was a double-pulsed solid-state Nd-YAG and had an output power of 120 mJ with a maximum pulse rate of 21 Hz. The images taken by the cameras were in the resolution of 1600×1186 pixels.

Perpendicular to the casting cell, the two CCD cameras were mounted in parallel. The PIV camera mount has a common housing with a shared observation window for the two cameras. This insures straightforward imaging of the same area of the flowing media, while allowing flexible camera positioning. To distinguish the flow from the moving crystals, a green filter was mounted on one CCD camera (band pass filter of 532 nm through which only laser light passes, which was scattered by the equiaxed crystals) and an orange filter on the other camera (high pass filter of 570 nm through which only the light passes, which was reemitted by the fluorescent dye (Rhodamine B)). In this way, the cameras captured images without ''interphase'' noise, which could then have been processed without any further treatment to obtain the two velocity fields. A set of 20 images was taken every 60 seconds and stored on a PC. The time separating two images was 0.25 seconds which was small enough to correctly catch the time variation of any motion.

III. RESULTS

In the Part I of the paper, different stages were described during the solidification process. The first regimes are only thermal: TH1 (when temperature is kept constant at 317.15 K (44 °C)), TH2 (just after start of cooling), and TH3 (at 8 minutes after the cooling started). The first and last thermal regimes are characterized by symmetric convection patterns, going up (TH1) or down (TH3) along the walls. The TH2 is an unstable transition stage. Once the solidification started, the regimes are driven by thermo-solutal convection. We distinguish then the perturbed thermal stage (PTH), the turbulent (TU) stage, the coherent chaotic (CC), and the meandering flow stage (MF). In this Part II of the paper, we will refer to these stages using the abbreviated forms, given above in brackets.

A. *Equiaxed Motion and Interaction with Melt Flow*

The interaction between the melt flow and the equiaxed crystals can be studied by comparing the horizontal and the vertical component of the crystals' velocity. Without any interaction with the flow, the

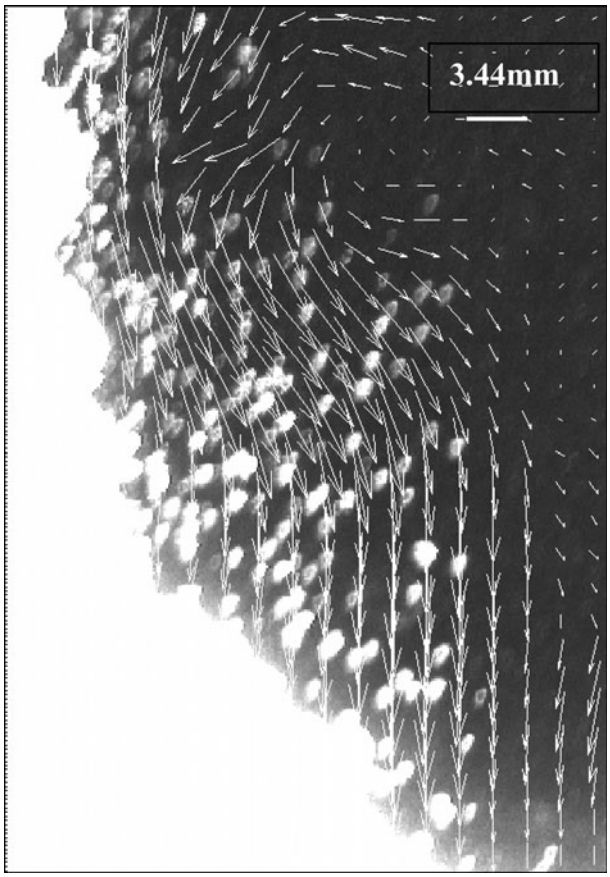

Fig. 1—Equiaxed crystal velocity field near the left solidification front at $t = 20$ min. The velocity vectors are scaled between $v_{min} = 0.28$ mm/s and $v_{max} = 3.76$ mm/s.

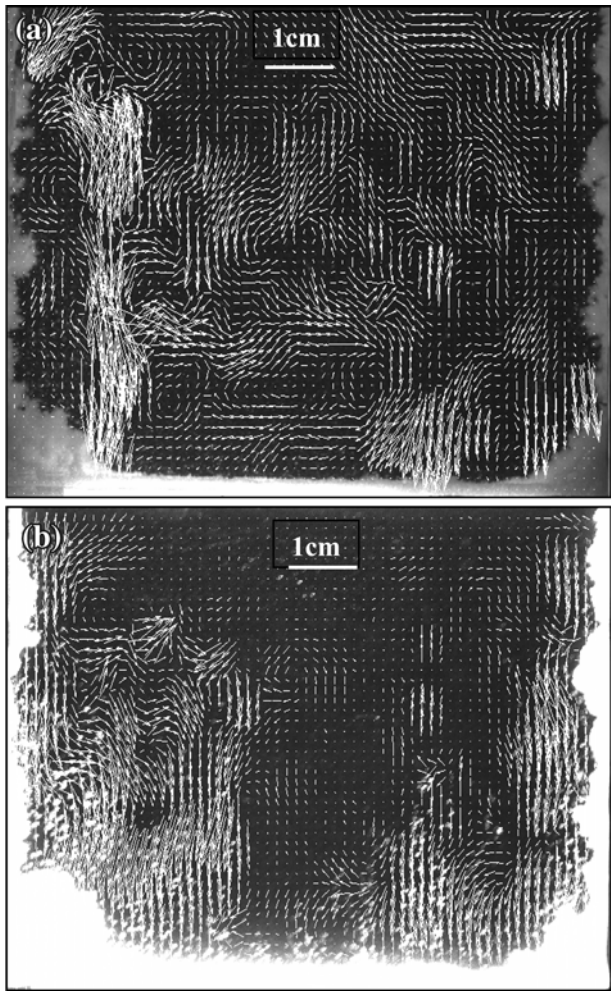

Fig. 2—Examples showing the melt velocities (*a*) and the equiaxed crystal velocities (*b*) for the so-called coherent chaotic regime (CC). The two-camera PIV measurement was done at $t = 15$ min. The velocity vectors are scaled between $v_{min} = 0.111$ mm/s and $v_{max} = 1.56$ mm/s for the liquid (a) and between $v_{min} = 0.278$ mm/s and $v_{max} = 3.87$ mm/s for the equiaxed crystals (b).

crystals would simply sink down. Therefore, the presence of a horizontal crystal movement is a direct indication of the interaction with the melt. The first observation is that even large crystals possess a horizontal velocity of typically 10 to 50 pct of the vertical velocity (Figure 1). In the upper part of the domain, where crystals are smaller than in the lower part, sometimes an upward motion was observed (Figures 2b and 3b). The quantification of the interaction between the melt flow and the equiaxed crystals is difficult,[20] but using the described two-camera PIV system, it is quite straightforward. We just estimated the vertical velocity difference between measured crystal velocity, $U_y^{crystal}$, and flow velocity, U_y^{flow}. To obtain accurate crystal velocities, it is necessary to choose an area where the number of crystals is large enough for the PIV correlation. In Figure 4, the vertical relative velocity at $t = 25$ minutes is plotted along three vertical lines, two located near the left and right solidification front and one near the center. It is obvious that the vertical relative velocity turns out to be irregular. The velocity difference is neither constant, nor increase linearly with the distance from the top surface. However, a power law or an exponential tendency can be noticed. This tendency is similar to that found by B. Appolaire et al.[21] for a single crystal falling in an undercooled liquid. It can be attributed to the increase in size of the crystal while falling. The equiaxed crystals surrounded by the undercooled liquid will grow,[21–23] while those which meet low concentrated liquid could experience melting.

The crystals' volume fraction increases during sedimentation. At the vicinity of the mushy zone, the numbers of crystals is high enough that an increase in inter-phase drag can be expected. The decrease of the typical crystal–crystal distance generates frictions so that the crystals and the liquid tend to equalize their velocities. In Figure 4, ΔU_y decreases over a distance of about 15 mm from the bottom solidification front. This phenomenon can be attributed to a change in drag regime, probably from a Stokes' to a porous kind of permeability law.[24] This explains the uniformity of the equiaxed crystals' flow field in all high crystal concentration areas, especially present in the vicinity of the solidification front (Figures 1, 2, 3). The same remark can be given in the stratified regime (MF) where the high density number of equiaxed forces the flow to reorient

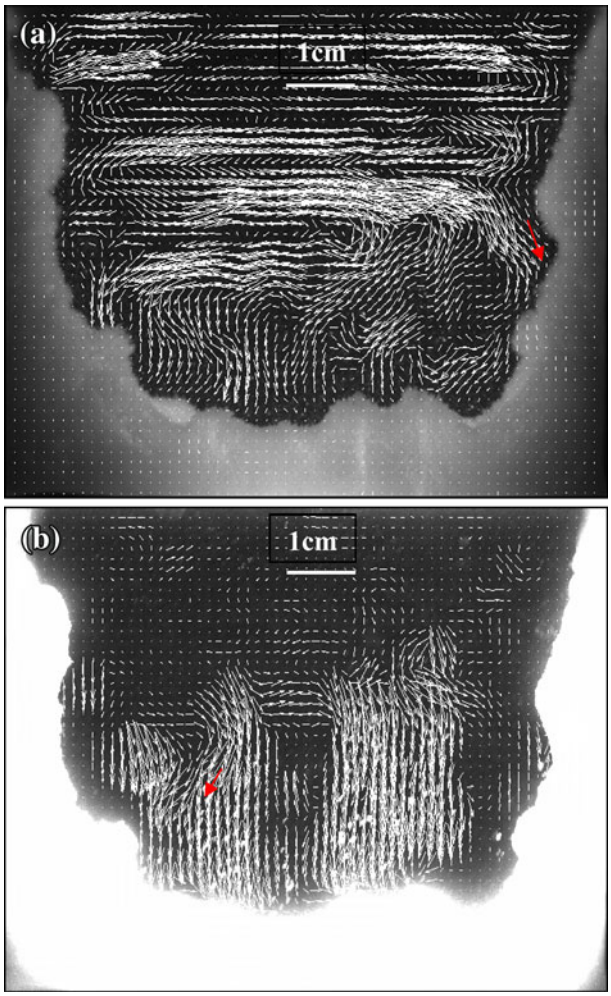

Fig. 3—Examples showing the melt velocities (*a*) and the equiaxed crystal velocities (*b*) for the meandering flow regime (MF). The two-camera PIV measurement was done at $t = 30$ min. The velocity vectors are scaled between $v_{min} = 0.067$ mm/s and $v_{max} = 0.466$ mm/s for the liquid (a) and between $v_{min} = 0.155$ mm/s and $v_{max} = 2.17$ mm/s for the equiaxed crystals (b).

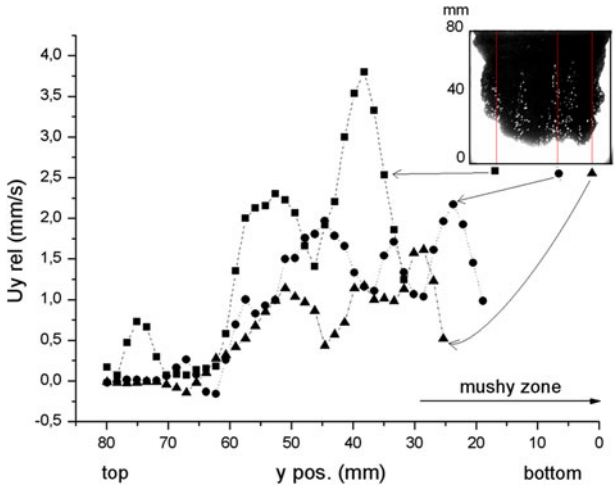

Fig. 4—Measured *Y*-component of the relative velocity along three vertical lines at $t = 25$ min (MF regime).

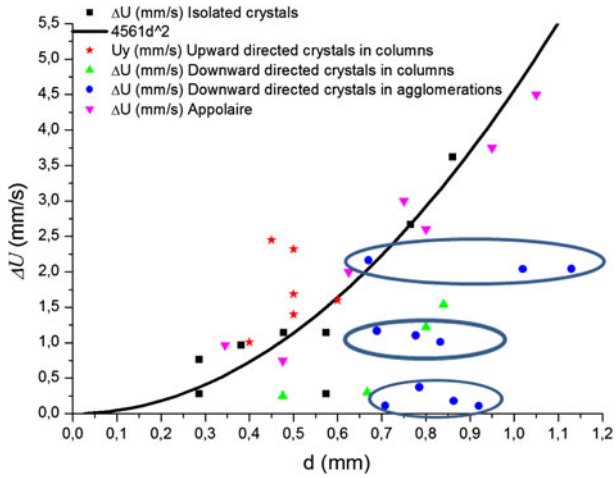

Fig. 5—Relative velocity for single crystals *vs* the crystal size (diameter), and a comparison between rising (red) and falling (green) velocity magnitude in chimneys (Color figure online).

and to finish its path in the downward direction through the mush.

The fundamental aspect is the relation between the relative velocity and the crystal size. Such a relation exists for a spherical particle and is known as Stokes' law. To check its validity for equiaxed crystals, it is necessary to extract the relative velocity for isolated crystals not in crystal agglomeration. In this case, as already mentioned, the use of picture correlation was not possible; so, the velocities were extracted by the particle tracking method.

To obtain precise results, it is better to choose a regime where the flow does not have a strong unsteady nature, and therefore we chose the regime MF for the following evaluation. At this regime, we can eliminate the influence of a strong time and space variation of the liquid velocity on the particle motion. In order to estimate the size of a single crystal, we simply counted the bright pixels representing the crystal. Here, it has to be mentioned that due to the light overexposure (necessary for acceptable PIV correlations) and the diffraction by the crystals, no morphological details of the equiaxed crystal were visible; the apparent size might be larger than the real size. In Figure 5, we have plotted the calculated relative velocity of a single crystal as a function of the measured size.

The results for the isolated crystals show an increase of the relative velocity with the measured size. The magnitudes of the relative velocities found for the corresponding sizes are very similar to those reported by Appolaire.[1,2] The correlation follows a clear power tendency. Based on the Stokes' law, the relative velocity of a compact sphere can be calculated by:

$$\Delta U = \alpha \cdot d^2, \qquad [1]$$

where α gathers the materials' properties (ρ_A the density of the sphere, ρ_W the density of the surrounding fluid, g the gravity constant, μ the dynamic viscosity of the fluid, and d is the diameter of the sphere) in one single factor.

Table I. Different Drag Coefficient Values Calculated for Measured Diameter Sizes and Relative Velocities

d (m)	ΔU (m/s)	Re	24/Re	C_D (Eq. [2])
3.82e−04	9.66e−04	4.34e−01	55.4	2.232e+03
2.86e−04	7.61e−04	2.56e−01	93.9	2.692e+03
4.78e−04	1.14e−03	6.42e−01	37.4	1.991e+03
7.648e−04	2.67e−03	2.40	10.0	5.85e+02
5.736e−04	2.79e−04	1.88e−01	128	4.0181e+04
2.86e−04	2.8e−04	9.41e−02	255	1.9891e+04
8.6e−04	3.62e−03	3.66	6.56	3.57e+02
5.736e−04	1.14e−03	7.69e−01	31.2	2.402e+03

Using the measured sizes and velocities, the particle Reynolds number $\mathrm{Re_P} = \frac{\rho_A \Delta U_y d}{\mu}$ is always smaller than 4 allowing the use of Eq. [1]. We have just used Eq. [1] to fit the experimental data of Figure 5. With the materials' properties given in Table I in the Part I of this paper, the value of α can be calculated to be 188402.3. However, the fit to the measuring points from Figure 5 gives $\alpha = 4561$. Thus, the computed relative velocity for spheres (0.01 m/s for $d = 0.75$ mm) is almost 41 times larger than the measured ones.

Due to the fact that the equiaxed crystals are not spherical, and due to their rough fractal surface, this was expected. This is the reason why in the past, numerical simulation was performed by means of modified drag laws to account for the equiaxed shapes.[25–29] These drag laws predict systematically larger drag coefficients C_D than for spheres. In our case, we calculated the drag coefficient C_D using the equation below:

$$C_D = \frac{4}{3}\frac{d\Delta\rho g}{\rho_W \Delta U^2}, \qquad [2]$$

The different drag coefficients calculated for the measured sizes and relative velocities for the single equiaxed crystals are presented in Table I. For Reynolds numbers between 10^{-1} and 10^{-2}, the results obtained for C_D cover a large range between 10^2 and 10^4. These values are very similar to those calculated by Tang[30] for particles having fractal surfaces.

Based on the experimental correction of Eq. [1], the equiaxed relaxation time is estimated to be:

$$\tau_e = \alpha \frac{\rho_A - \rho_W}{\rho_A} d^2 \leq 10^{-4}\mathrm{s}, \qquad [3]$$

Compared to the measurement frequency (250 ms), it is very small. It can be assumed that the crystals instantaneously reach their terminal relative velocity. Thus, the polynomial increase of ΔU_y observed in Figure 4 can be directly related to the growth of volume during the crystal fall. A linear or quadratic growth of the crystal diameter with time, as observed by Appolaire,[21,22] could easily reproduce the measured acceleration along the vertical direction (Figure 4).

The local maximum equiaxed volume fraction was estimated by the ratio of the volume of the crystals to the total volume. It was found smaller than 10 pct. Nevertheless, in this area of higher crystal number density, columns, and agglomerations, no clear correlation can be extracted; the results are very dispersed, see blue points in Figure 5. Smaller crystals can have higher relative velocities than larger ones. It can be observed that the same relative velocity can be reached by different crystal sizes. The blue points (crystals in agglomeration) are arranged along three lines where the crystals have different sizes, but approximately the same relative velocity. The crystals are slowed down by the presence of neighboring crystals; a higher solid fraction is known to increase the apparent viscosity. This situation occurs within the large and dense crystal clouds near the solidification front (agglomerations) or even in the bulk flow (columns or chimneys). The mechanism of momentum exchanges between the two phases might be controlled by some intermediate drag laws between the free particle regime and the packed bed regime where the crystals are almost not moving.

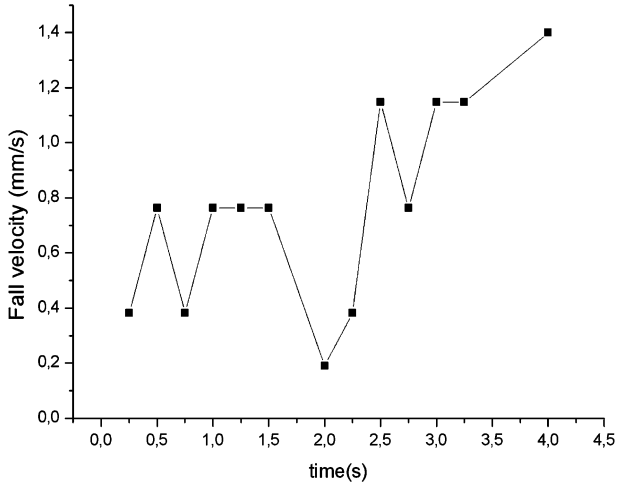

Fig. 6—Time evolution of the falling velocity of a single crystal ($d \sim 0.3$ mm) within a chimney at $t = 20$ min.

By comparing Figures 2(a) and (b), we can notice that variations of the liquid velocities are smoother in areas where a large number of equiaxed crystals exist. This phenomenon is particularly visible if we compare the flow coherence in the bulk with the high equiaxed number density regions. The flow in these regions is well structured in clear streamlines or in large eddies. Obviously, the presence of crystals' motion through drag interaction damps the turbulence eddies. We can suppose that due to the extension of the area of falling crystals and the decrease in magnitude of ΔC, a laminarization of the entire domain occurs, leading to a transition to the laminar chaotic regime (Figure 2).

B. *Equiaxed Motion in Solutal Flow Chimneys*

During the turbulent and chaotic regimes, equiaxed crystals are constantly accelerating or decelerating. In Figure 6, the falling velocity of a single crystal, in a chimney, at $t = 20$ min is plotted along the time until it hits the mushy zone. During this time, its appearing size was almost constant (it increased from 0.3 mm to 0.34 mm). This unstable behavior leads to the idea that

under such conditions, even for an isolated crystal, other forces might act on the crystal. The nonisotropic shape of the small crystals can generate rotation, and can cause a non-negligible lift action in regions with strong velocity gradients. It is also possible that eddies smaller than interrogation area sizes (0.16 mm), thus not fully caught in the flow map, act on the crystals in a quasi-random manner. If it exists, this phenomenon is believed to happen only during the turbulent regime, and near the solute jet in flow chimneys.

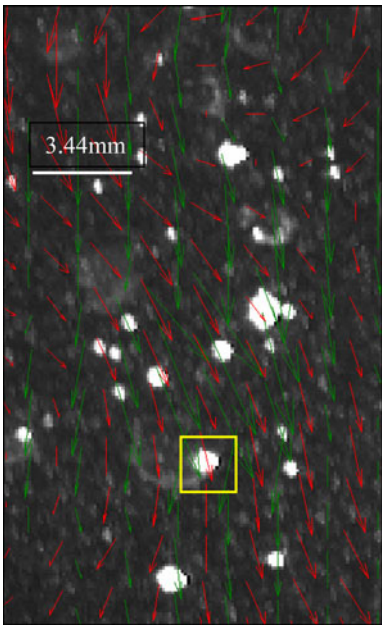

Fig. 7—Crystals and liquid velocities map within a chimney obtained by an adaptive-correlation technique at t = 23 min. Notice that the adaptive-correlation technique shows only downward vectors, although a rising crystal (marked by yellow square) is present. The velocity vectors are scaled between v_{min} = 0.04 mm/s and v_{max} = 0.16 mm/s for the liquid (red vectors) and between v_{min} = 0.525 mm/s and v_{max} = 2.27 mm/s for the equiaxed crystals (green vectors) (Color figure online).

These flow chimneys visible in Figures 7, 8, and 9 are the results of solute jets generated in the mushy zone, also called flow chimneys or columns. Most of the visible crystals fall downward, but some are rising upward at a higher speed (Figures 7 and 8). On one hand, the cross correlation method cannot catch this upward movement since this motion concerns only few crystals. On the other hand, due to the too short distance between the crystals, the particle tracking method can hardly be used to follow each moving crystal. The rising velocities' magnitudes reported in Figure 5 were directly calculated by measuring the displacement of the chosen crystal on the images. Owing to the presence of a strong solutal jet, the upward velocities are typically larger than the measured downward velocities (Figure 5). Unfortunately, the thin solute jet is not visible on the liquid velocity map. The 16 × 16 pixels resolution corresponding to a 2D 0.08-mm resolution is believed to be accurate enough to resolve the jet. In some experiments, no rising crystals were observed within the chimney, meaning that the jet was not illuminated by the laser light. However, even if a jet is localized within the 1-mm-thick laser plane, the volume of surrounding downward velocities (flow and crystal) will have a higher impact on the results of the correlation. The jet will be invisible from the flow velocity and crystal velocity map (Figure 7).

In the opposite to the lower parts of the chimneys, where the flow and the crystals' velocities are almost collinear, in the higher parts, the relative velocity can be very large. Sometimes, the measured liquid flow is almost perpendicular to the crystal flow. In Figure 9, the crystal

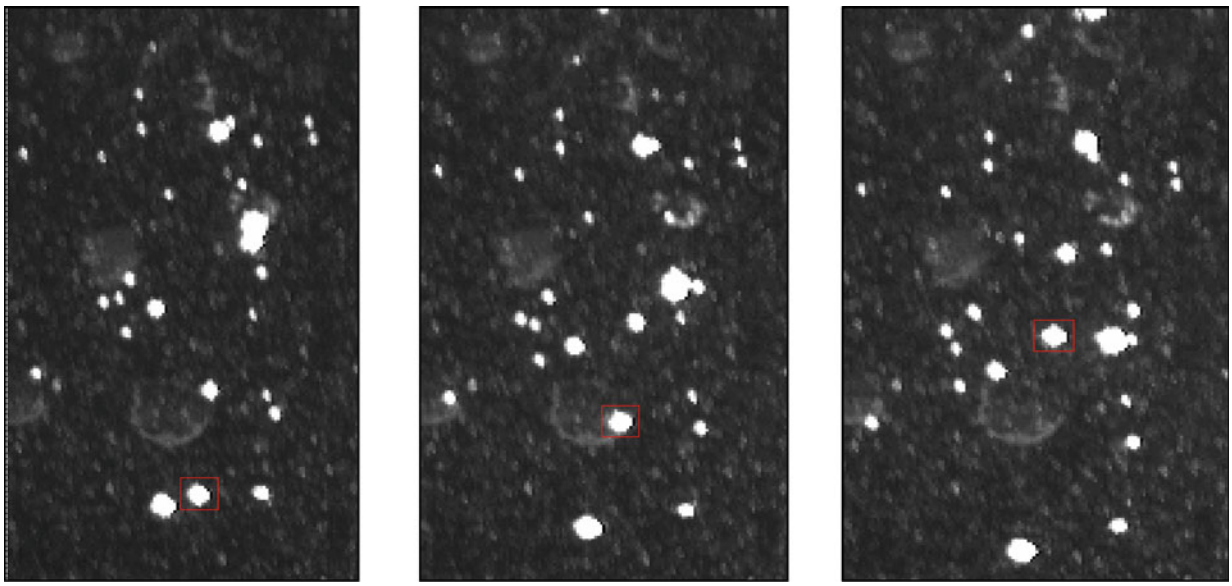

Fig. 8—Movement of an upward moving crystal surrounded by falling crystals at t = 23 min. The pictures show a zoom-in area of 12 × 20 mm^2.

moving within a chimney acts almost as a porous wall. It is clear that the two phases behave differently from what could be predicted by means of simple Stokes' drag law. By following the flow path, we can observe that a part of the liquid goes through and another part of the liquid flow is clearly reflected. If a chimney is interrupted at a certain height, the liquid will choose to flow through this interruption.

A collision between rising and falling crystals occurs (Figure 10). After the collision, the two crystals can coalesce in one single crystal and fall down. By considering the speed and the size of the two objects, the collision does not seem to respect the simple form of the momentum conservation law. Perhaps the kinetic energy has been absorbed by some viscous, thermodynamically or porosity-related phenomena. However, these collisions are relatively rare and surprisingly more frequent in diluted regions and never observed in high concentrated regions.

C. *Meandering Flow*

Due to its opacity, the flow through the mushy media is invisible. Nevertheless, in Figure 3a, the meandering flow starting from the top vanishes at the bottom mushy zone. The question is how the flow closes its streamlines. It is also possible that the closure is made along the front and the back glasses. At the end of the process, when the liquid reaches about 285.15 K (12 °C), the external room temperature 297.15 K (24 °C) can promote buoyant upward flow at these two walls. However, the flow map and the mass conservation suggest that this meandering flow closes its path through the mushy zone.

At the end of the experiment, the mushy zone represents 28 pct of the cell volume. According to the phase diagram, only 8 pct of the NH_4Cl mass will solidify. If the entire concentration solidifies in a packed form, it can fill only 6 pct of the cell volume. A simple calculation gives that in average, the mushy zone contains about 25 pct of solid and 75 pct of liquid. However, this is only an average value, the real solid fraction might be much higher at the vicinity of the cold wall and much lower near the solidification front. While the flow enters openly within the bottom mushy zone, it is deviated and curved by the solidification front surface. The vertical mushy regions act almost as nonpermeable media. Perhaps the fact that the vertical mushy regions are built with a succession of equiaxed and columnar layers might explain the difference with the bottom mushy layer. In addition, the sizes of equiaxed crystals that participate in the growth of the vertical walls are smaller than the ones reaching the bottom regions. Using a similarity between packed crystals and packed spheres, the Black-Kozeny law[24,25,31] predicts that the permeability increases with the crystals' size. These considerations, together with the flow observation, confirm that a strong variation in effective permeability (and porosity) might exist specially all over the surface of the solidification front.

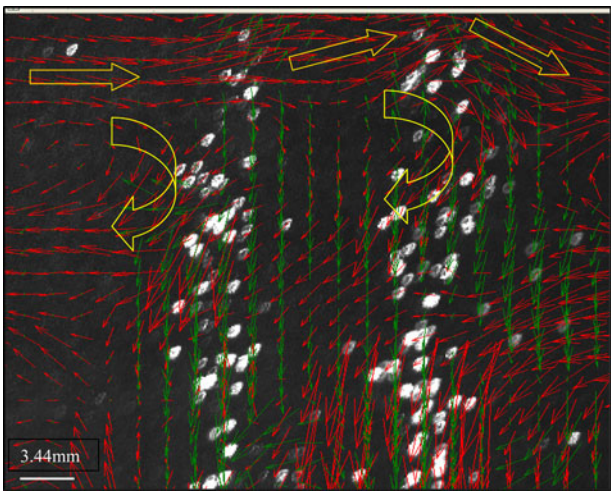

Fig. 9—Superimposition of the liquid melt flow and equiaxed crystals' motion filled in top chimneys at t = 20 min. The velocity vectors are scaled between v_{min} = 0.178 mm/s and v_{max} = 2.49 mm/s for the liquid (red vectors) and between v_{min} = 0.782 mm/s and v_{max} = 3.387 mm/s for the equiaxed crystals (green vectors) (Color figure online).

IV. CONCLUSIONS

A special particle image velocimetry technique was used to measure the velocity field during a columnar/equiaxed solidification process. The single-phase measurement technique developed for PIV has been extended to cope with liquid-equiaxed flows. It was applied to H_2O-NH_4Cl solidification in a die cast cell of $10 \times 10 \times 1$ cm^3 in which both the liquid velocity and the crystals' velocity maps could be extracted. The separation between the two velocity fields could be

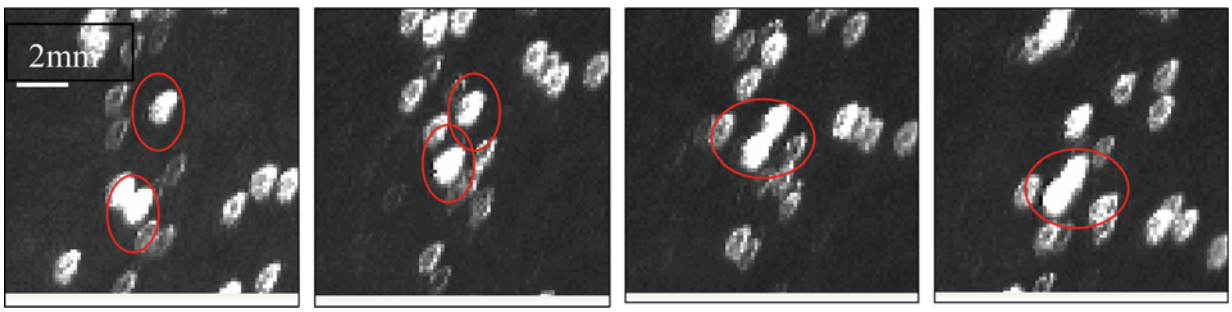

Fig. 10—Collision and coalescence of two crystals. Initial distance between the two crystals ~2 mm, t = 24 min.

obtained with the use of fluorescent particles' tracers that emit different waves when excited with the laser wavelength. Two images were taken simultaneously with two different cameras; the first one recorded only the laser light through a green filter, while the second one used an orange filter to record only waves emitted by the fluorescent particles. Thus, the first camera could follow only the trajectories of crystals, while the second camera recorded the liquid velocity field.

In general, no clear relation was found between the size and the settling velocities of the crystal. However, isolated crystals were found to fall 41 times slower than spheres of equivalent apparent sizes. In agreement to what is generally believed, only a drag coefficient larger than one can explain such velocities. Perhaps the origin of this phenomenon could be found in the fractal shape of the crystal.

The coupling between the fluid flow and the equiaxed crystal was found to be important in the area of high crystal number density; the two phases have often collinear velocity fields. In these regions, the liquid flow has shown smoother velocity variations than in the chaotic or the turbulent bulk. This observation is proof that equiaxed crystals tend to damp a part of the turbulence. Simultaneously, the velocities in the bulk flow were found to accelerate during the period of strong crystal fall near the vertical walls. When the region of equiaxed rain shifted to the bulk flow, the velocity magnitudes dropped strongly. This experience leads to the idea that the equiaxed motion has not only a stabilizing effect, but also can be a source of momentum acceleration. Perhaps in larger systems as in industrial scale, a generation of turbulence could be observed. This indicates that very complex behaviors can be expected from the interaction between flow and solidification in larger systems.

ACKNOWLEDGMENTS

We kindly acknowledge the FWF (Austrian Science Fund, grant number P17619-N02 and P22614-N22) which paid the PhD scholarship for Mrs. Stefan-Kharicha who performed the experiences, measurements, and calculations.

REFERENCES

1. C. Beckermann and R. Viskanta: *Appl. Mech. Rev.*, 1993, vol. 46, pp. 1–27.
2. C. Beckermann:, in *International Conference on Modeling of Casting, Welding and Advanced Solidification Processes VI*, T.S. Piwonka, V. Voller, and L. Kategerman, eds., TMS, Pennsylvania, Warrendale, 1993, pp. 181–192.
3. M. Rappaz: *Int. Mater. Rev.*, 1989, vol. 34, pp. 93–123.
4. R.A. Gore and C.T. Crowe: *J. Fluid Eng. T. ASME*, 1991, vol. 113, pp. 304–07.
5. G. Hetsroni: *Int. J. Multiph. Flow*, 1989, vol. 15, pp. 735–46.
6. D.A. Kalitov and E.K. Longmire: *Exp. Fluids*, 2002, vol. 32, pp. 252–68.
7. A. Kitagawa, Y. Hagiwara, and T. Kouda: *Exp. Fluids*, 2007, vol. 42, pp. 871–80.
8. G. Montante and F. Magelli: *Ind. Eng. Chem. Res.*, 2007, vol. 46, pp. 2885–91.
9. T. Virdung and A. Rasmuson: *Proceedings of the 11th European Conference on Mixing*, VDI-GVC, Bamberg, Germany, 2003, pp. 129–136.
10. FLUENT 6.3: *User's Guide*, Fluent Inc., Lebanon, NH, 2006.
11. C. Beckermann and C.Y. Wang: *Metall. Mater. Trans. A*, 1996, vol. 27A, pp. 2784–95.
12. C.Y. Wang and C. Beckermann: *Metall. Mater. Trans. A*, 1996, vol. 27A, pp. 2754–64.
13. C.Y. Wang and C. Beckermann: *Metall. Mater. Trans. A*, 1996, vol. 27A, pp. 2765–83.
14. R.J. Adrian: *Ann. Rev. Fluid Mech.*, 1991, vol. 23, pp. 261–304.
15. Z.-C. Liu, C.C. Landreth, R.J. Adrian, and T.J. Hanratty: *Exp. Fluids*, 1991, vol. 10, pp. 301–12.
16. C. Willert, B. Stasicki, M. Raffel, and J. Kompenhans: *SPIE Proc.*, 1995, vols. 2546–2519, pp. 32–39.
17. K. Okamoto and M. Oki: *International Conference on Advanced Optical Diagnostics in Fluids, Solids and Combustion*, Tokyo, Japan, 2004, pp. 1–5.
18. Y.A. Hassan, W.D. Schmidl, and J. Ortiz-Villafuerte: *J. Vis.*, 1998, vol. 1, pp. 291–301.
19. Y.M.C. Delauré, V.S.S. Chan, and D.B. Murray: *Exp. Therm. Fluid Sci.*, 2003, vol. 27, pp. 911–26.
20. C. Beckermann, C. Fan, and J. Mihailovic: *Int. Video J. Eng. Res.*, 1991, vol. 1, pp. 71–82.
21. B. Appolaire, V. Albert, H. Combeau, and G. Lesoult: *ISIJ Int.*, 1999, vol. 39, pp. 263–270.
22. B. Appolaire, Ph.D., INPL, 1999.
23. C. Bizon, J. Werne, A.A. Predtechensky, K. Julien, W.D. McCormick, J.B. Swift, and H.L. Swinney: *Chaos*, 1997, vol. 7, pp. 107–24.
24. C.Y. Wang, S. Ahula, C. Beckermann, and H.C. de Groh III: *Metall. Mater. Trans. B*, 1995, vol. 26B, pp. 111–19.
25. A. Badillo, D. Ceynar, and C. Beckermann: *J. Cryst. Growth*, 2007, vol. 309, pp. 197–215.
26. A. Badillo, D. Ceynar, and C. Beckermann: *J. Cryst. Growth*, 2007, vol. 309, pp. 216–24.
27. B. Appolaire, H. Combeau, and G. Lesoult: *Mater. Sci. Eng., A*, 2008, vol. 487, pp. 33–45.
28. M. Wu and A. Ludwig: *Acta Mater.*, 2009, vol. 57, pp. 5621–31.
29. M. Wu and A. Ludwig: *Acta Mater.*, 2009, vol. 57, pp. 5632–44.
30. P. Tang, H.-K. Chan, and J.A. Raper: *Powder Technol.*, 2004, vol. 147, pp. 64–78.
31. N. Zabaras and D. Samanta: *Int. J. Num. Methods Eng.*, 2004, vol. 60, pp. 1103–1138.